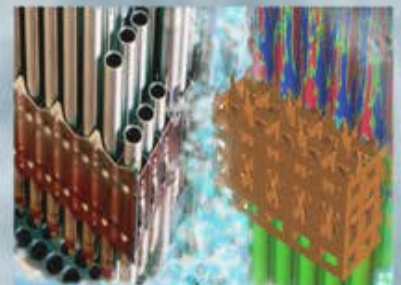
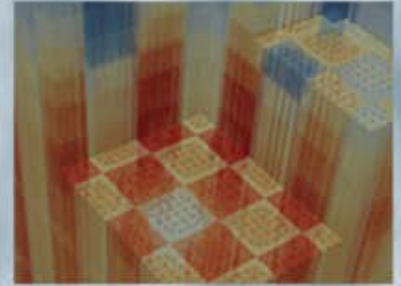


IR-THERMOGRAPHY-BASED INVESTIGATION OF CRITICAL HEAT FLUX IN SUBCOOLED FLOW BOILING OF WATER AT ATMOSPHERIC AND HIGH PRESSURE CONDITIONS

A. Richenderfer, MIT
A. Kossolapov, MIT
Jee H. Seong, MIT
M. Bucci, MIT
J. Buongiorno, MIT

March 23, 2017

Approved for Public Release



Please complete sections appropriate for this record.

REVISION LOG

| Revision | Date | Affected Pages | Revision Description |
|----------|------------|----------------|----------------------|
| 0 | 03/27/2017 | All | Initial Release |
| | | | |
| | | | |
| | | | |

Document pages that are:

Export Controlled None

IP/Proprietary/NDA Controlled None

Sensitive Controlled None

Unlimited All

Requested Distribution:

To:

Copy:

**IR-THERMOGRAPHY-BASED INVESTIGATION OF
CRITICAL HEAT FLUX IN SUBCOOLED FLOW
BOILING OF WATER AT ATMOSPHERIC AND HIGH
PRESSURE CONDITIONS**

A. Richenderfer, A. Kossolapov, Jee H. Seong, M. Bucci*, J.
Buongiorno

Department of Nuclear Science and Engineering
Massachusetts Institute of Technology, Cambridge, MA, USA

*mbucci@mit.edu

Consortium for Advanced Simulation of Light Water Reactors (CASL)

Report for Milestone L3:THM.CLS.P14.02

(Rev. 1)

March 23, 2017

Abstract

Here we report on MIT's THM work in Q4 2016 and Q1 2017. The goal of this project is to design, construct and execute tests of flow boiling critical heat flux (CHF) at high-pressure using high-resolution and high-speed video and infrared (IR) thermometry, to generate unique data to inform the development of and validate mechanistic boiling heat transfer and CHF models.

In FY2016, a new test section was designed and fabricated. Data was collected at atmospheric conditions at 10, 25 and 50 K subcoolings, and three mass fluxes, i.e. 500, 750 and 1000 kg/m²/s. Starting in Q4 2016 and continuing forward, new post-processing techniques have been developed to analyze the data collected. These new algorithms analyze the time-dependent temperature and heat flux distributions to calculate nucleation site density, nucleation frequency, growth and wait time, dry area fraction, and the complete heat flux partitioning.

In Q1 2017 a new flow boiling loop was designed and constructed to support flow boiling tests up to 10 bar pressure and 180 °C. Initial shakedown and testing has been completed. The flow loop and test section are now ready to begin high-pressure flow boiling testing.

1. Introduction and Objectives

In Pressurized Water Reactors (PWRs), the core inlet condition of the flow is highly subcooled to prevent saturated boiling in the core. However, subcooled flow boiling is possible during normal operating conditions and particularly during transients, such as loss of flow. Under such conditions even departure from nucleate boiling is possible. Understanding and accurately modeling boiling heat transfer for the complete nucleate boiling curve, including the departure from nucleate boiling (DNB) condition, is crucial for the improvement of the design and safety of current and future nuclear reactors.

The aim of this work is to better understand the mechanisms and partitioning of the heat flux in subcooled flow boiling condition up to CHF. To that end, we designed an experiment to capture flow boiling phenomena with high-resolution, and generate a database for the development and validation of mechanistic boiling heat transfer models and simulations.

The report describes activities performed over the past year of the project. Design and fabrication of the new test section, improvement of the experimental apparatus, shakedown of the flow loop and results from the tests conducted to date are discussed.

Scope of Work

The focus of this year's campaign is the design, shakedown and execution of flow boiling experiments (up to and including CHF) in pressurized conditions (up to 10 bars pressure). To do so, a new flow loop was required to accommodate high-pressure and high-temperature testing. Additionally, efforts were made to improve the water quality by introducing enhanced filtering and degassing systems. The new loop was paired with the test section designed and constructed during last year's campaign. A complete shakedown of the facility and development of standard operating procedures are near completion.

In addition to the collection of high-pressure data, new data post-processing algorithms are under development to analyze the atmospheric flow boiling data. These algorithms analyze the time-dependent temperature and heat flux distributions recorded by the IR camera, and quantify boiling heat transfer parameters and the complete heat flux partitioning. The new post-processing algorithms have been applied to the data collected in FY2016, and will be applied to the high-pressure data as part of this year's campaign.

2. Design of the New Test Section

In order to safely reach CHF a new test section was designed, as shown in Figure 1. The body of a test section is made of 316 stainless steel. It has three openings to accommodate quartz windows and one opening for the installation of the heater cartridge. Both windows and the heater cartridge are held in place by stainless steel flanges. PolyTetraFluoroEthylene (PTFE, also known as Teflon®) gaskets allow for the uniform distribution of a force upon tightening. Silicone O-rings are used to create a pressure boundary between the windows and test section body. Table 1 presents range of operating conditions for the new test section.

Figure 2 shows the arrangement of the heater cartridge. The body of the cartridge is made of Shapal®. Stainless steel side clamps push the heater to create a seal between the cartridge body and the heater. Such a design allows for a quick replacement of the heater if required. Copper leads are connected from behind and are used to supply electrical power to the heater. However, aluminum tape has since been used as it provides equally reliable electrical contact and flexibility without degrading the silver film. The use of clamps and O-ring for the heater installation provides the degrees of freedom required to accommodate the thermal expansion of the heater substrate, and reduces the risk of thermal shock.

Table 1 New test section operating conditions

| Parameters | Range |
|---------------------|------------------------------|
| Pressure | ambient to 10 bar |
| Temperature | ambient to saturation |
| Mass Flux | 0 – 2000 kg/m ² s |
| Reynolds Number | 0 – 60,000 |
| Subcooling | 0 – 75K |
| Heat Flux | 0 - 20 MW/m ² |
| Hydraulic Diameter | 1.5 cm |
| Boiling Number | 0 - 0.019 |
| Prandtl Number | 1.25 – 6.13 |
| Equilibrium Quality | -0.1 - 0 |

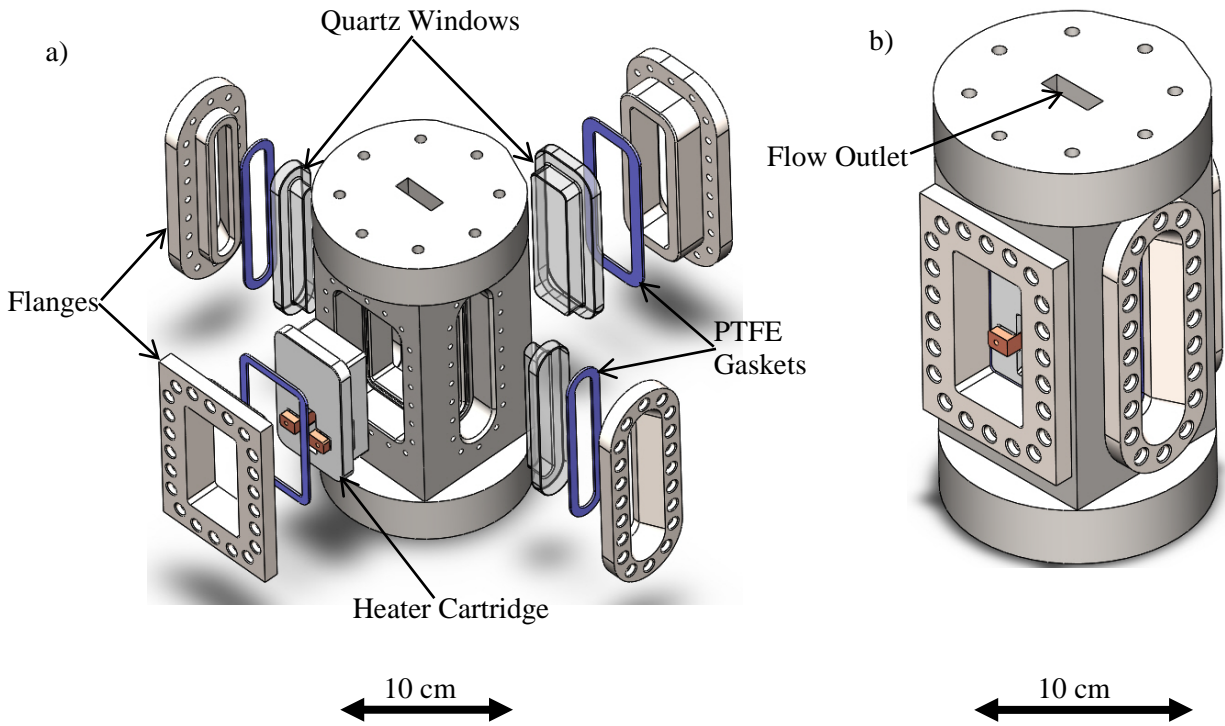


Figure 1. New test section design. Exploded (a) and assembled (b) views

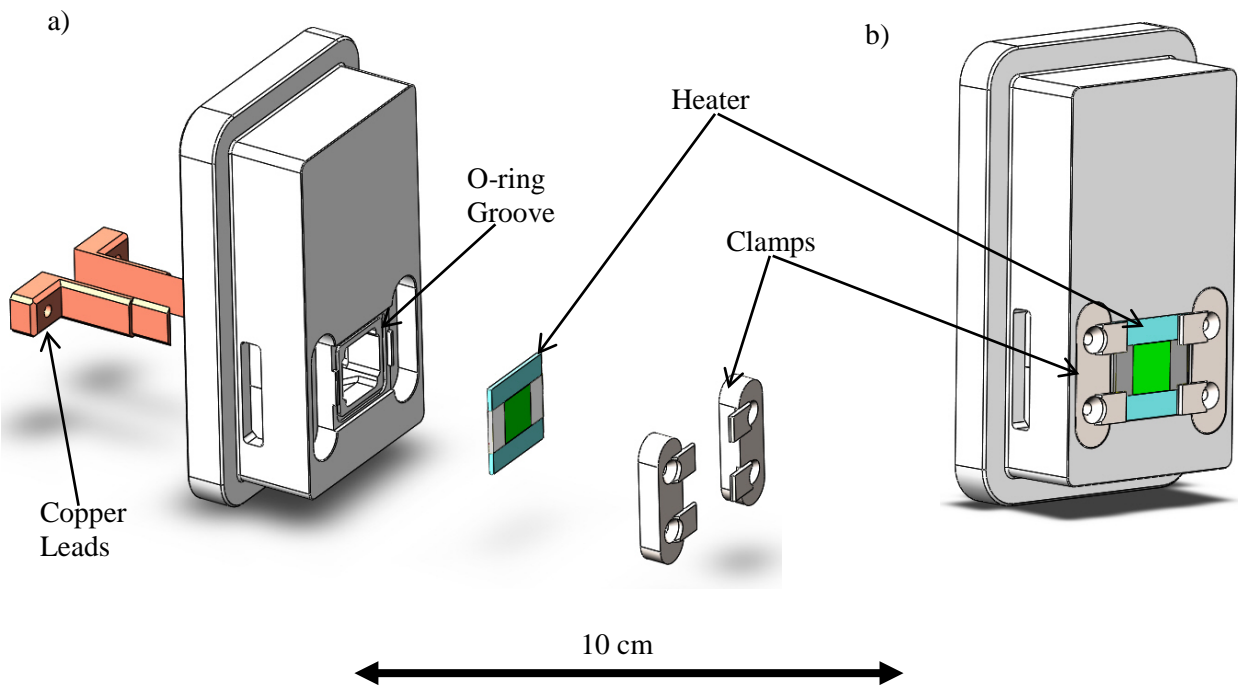


Figure 2. Exploded (a) and assembled (b) views of heater cartridge

3. Design of the heater

The combination of relatively high pressures (up to 10 bar) and thermal stresses induced from CHF conditions lead to significant mechanical and thermal stresses. Based on previous experience, we selected sapphire as a heater substrate for its resistance to such stresses. Figure 3 shows the heater design. The sapphire substrate is a 20x20 mm² square, 1-mm thick. Indium tin oxide (ITO) is wrapped around the substrate and serves as a heater. The ITO coating is opaque in the 3-5 μm wavelength range and transparent in the visible wavelengths. This allows an IR camera to image the ITO coating to collect data on the temperature and heat flux, while simultaneously allowing a high-speed video camera to image the heater from the top with an LED lighting the surface from behind. The ITO is nano-smooth and has a thickness of 0.7 μm and a resistivity of 2.5 Ohm/sq. Silver pads are deposited on top of the ITO and wrap around the filleted edges of the sapphire substrate. They limit the active ITO area to a 10x10 mm² square and allow a uniform supply of electric power to the heater surface.

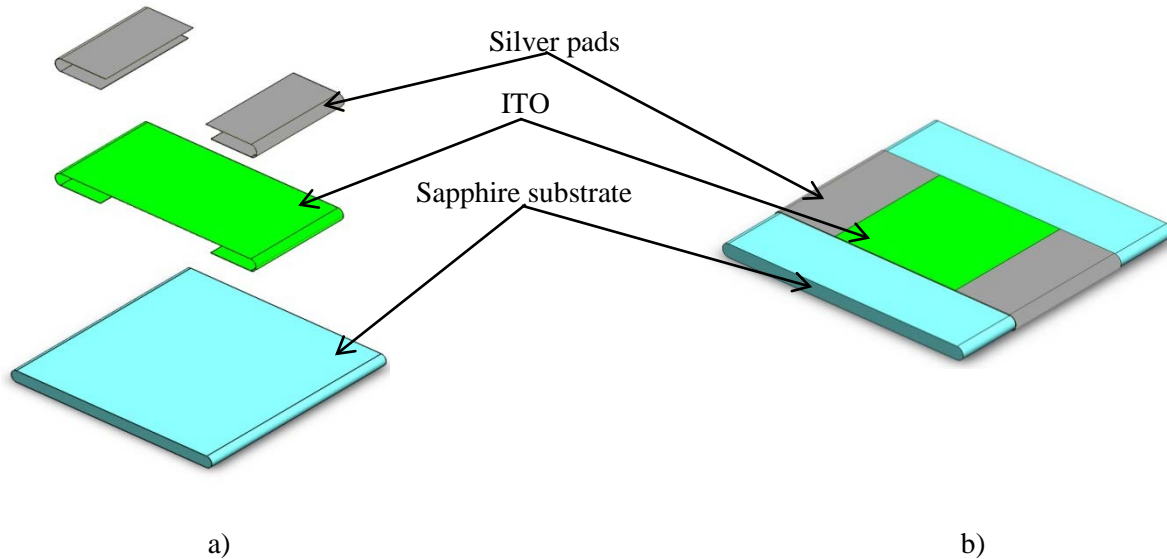


Figure 3. Exploded (a) and assembled (b) views of the heater

4. High-Pressure Flow Boiling Facility

The Platform for Experimental THERmal-hydraulics (PETHER) is an experimental flow boiling facility designed, constructed and operated in MIT's Nuclear Science and Engineering Department. The facility consists of two parts, a test section column and the supporting flow loop.

The flow loop is constructed using 316 stainless steel fittings and tubing. The loop is outfitted with a variable speed pump, a heat exchanger, accumulator, preheater, flow meter, and fill and drain tank along with accompanying temperature and pressure instrumentation.

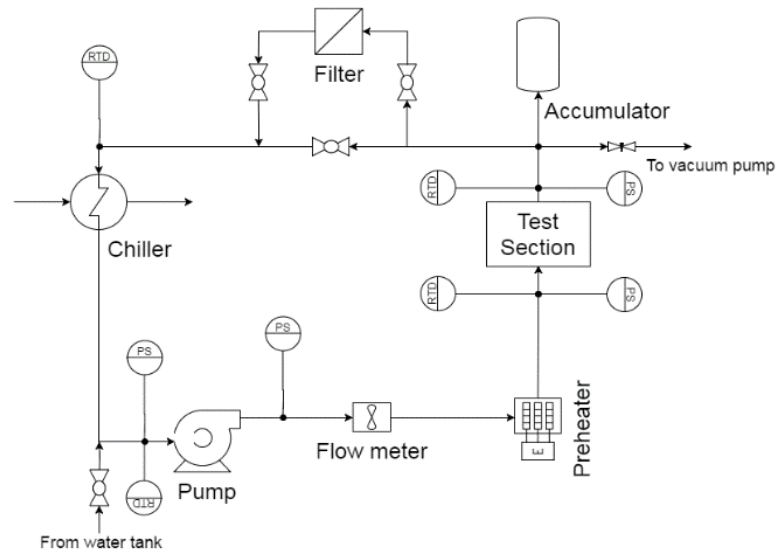


Figure 4. Flow Loop Diagram

Water filtering and dissolved oxygen removal systems are implemented via a secondary loop during the initial stages of testing. The loop supports flow rates up to $2000 \text{ kg/m}^2\text{s}$, and flow conditions up to saturation conditions at 10 bar pressure. Control and data acquisition are accomplished via an Agilent data acquisition system coupled with a Labview script.



Figure 5. Picture of high-pressure flow loop facility

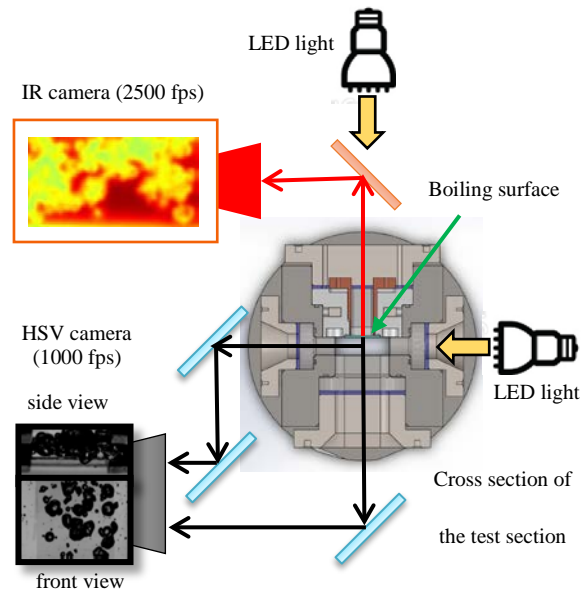


Figure 6. Optical arrangement of test section and cameras

5. Experimental Methods and Results

The data reported in this paper was collected at 10 K subcooling and atmospheric pressure. Prior to testing, the bulk flow was filtered and degassed. The heater surface was degassed by applying a moderate heat flux to initiate nucleate boiling and remove non-condensable gasses.

Data was acquired at three mass fluxes, 500, 750 and 1000 kg/m²s. For each flow condition, data collection started before the onset of nucleate boiling, at an applied heat flux of 100 kW/m² and

incremented slowly through the nucleate boiling curve. At each interval, a one second video was recorded of steady-state nucleate boiling. That is, 2500 frames of IR video and 10000 frames of HSV were recorded for each heat flux. At critical heat flux (CHF), a longer four-second video was recorded to capture the formation and evolution of the dry spot. Each set of flow conditions, resulting in one nucleate boiling curve, was repeated a second time to ensure experimental repeatability of the results.

The collected IR and HSV data for each flow condition and heat flux are post-processed using in-house scripts. In particular, the calibration of the IR data requires a coupled radiation-conduction model to analyze the temperature distribution within the heater and radiometric contributions from the sapphire and surrounding environment from the *a priori* measured optical properties as outlined by Bucci *et al.* [Bu2016]. The output of the calibration model is the 2-D surface temperature distribution and the 2-D surface heat flux distribution for each recorded frame. An example output of the radiation-conduction model is shown in Fig. 7.

Boiling curves (see Fig. 8) are measured using the time and space averaged temperature and heat flux distributions over the length of the recorded video (one second, 2500 frames). The error bars reported represent the standard deviation of the recorded temperature. Uncertainties associated with the recording of the camera are negligible compared to the time fluctuations of the temperature.

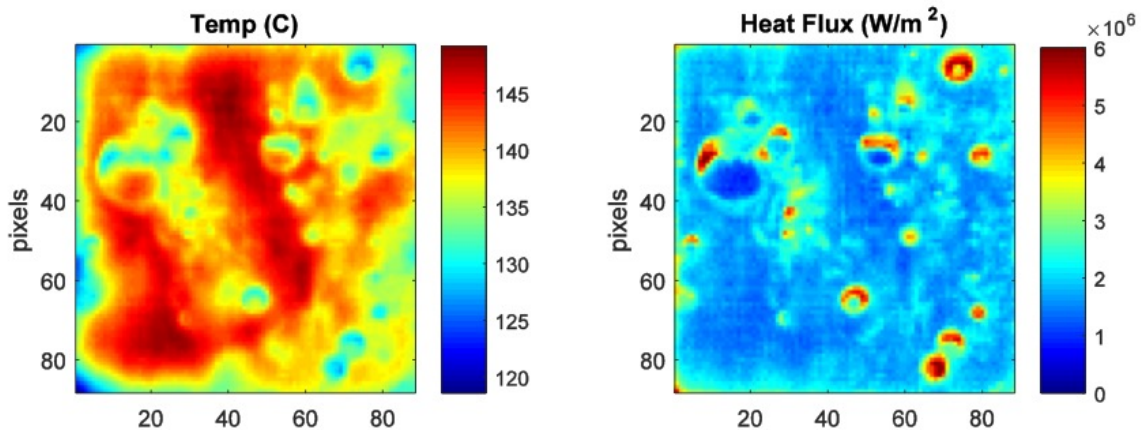


Figure 7. Typical output of radiation-conduction algorithm. (Each pixel corresponds to $115 \times 115 \mu\text{m}^2$)

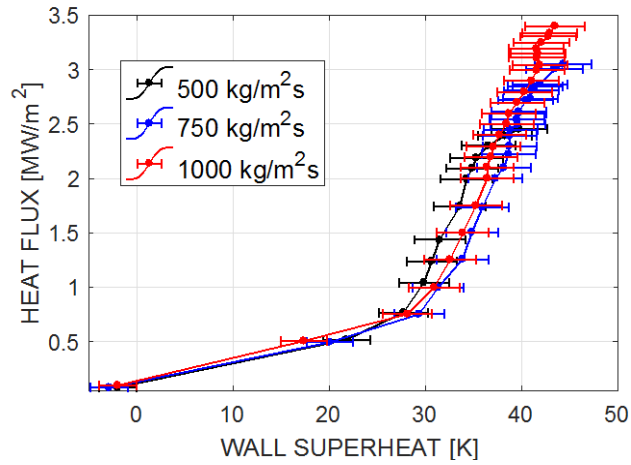


Figure 8. Boiling Curves for tests at 10K subcooling and 1 atm pressure

5.1 Critical Heat Flux

At each flow condition data was collected throughout the nucleate boiling curve. Once CHF was reached, a longer video was recorded to capture the establishment and growth of the dry spot. Below is a direct visualization of the DNB phenomenon.

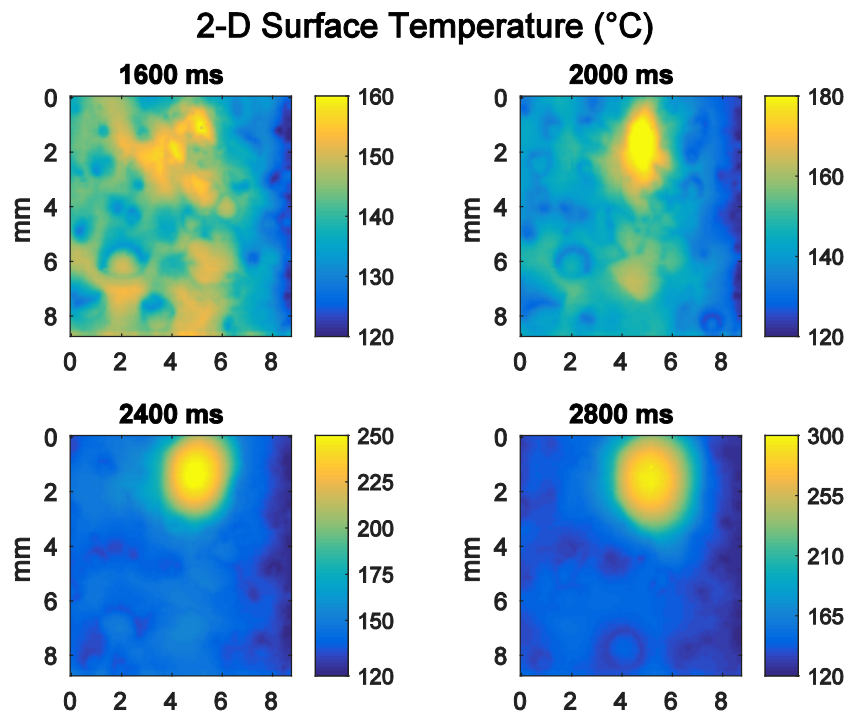


Figure 9. Temperature evolution of the dry spot during critical heat flux.

The recorded CHF values for the data reported here are shown in Table 1 along with the values from the Groeneveld look-up table [Gr2007].

| Mass Flux (kg/m²s) | 500 | 750 | 1000 |
|--|------------|------------|-------------|
| Recorded CHF (kW/m²) | 2450 | 3050 | 3400 |
| Groeneveld CHF (kW/m²) | 2604 | 2727 | 2823 |

Table 1. Recorded critical heat flux values and the equivalent look-up table values.

6. Post-Processing Techniques and Results

To effectively generate the required input for validation of a mechanistic boiling heat transfer model, the IR and HSV raw data must be post-processed to extract the important boiling heat transfer parameters. To do so, a series of algorithms were developed and applied to the data presented in Section 3. This section outlines the algorithms used and the results of the post-processing as they apply to the validation of new mechanistic models.

6.1 Nucleation Site Density

The nucleation site density was measured using two independent methods. First, the heater was imaged using a high-resolution microscope before testing began. The heater was then re-imaged after testing to reveal the areas where boiling occurred. A visual discoloration of the surface occurs where repetitive nucleation occurs as seen in Fig. 10.

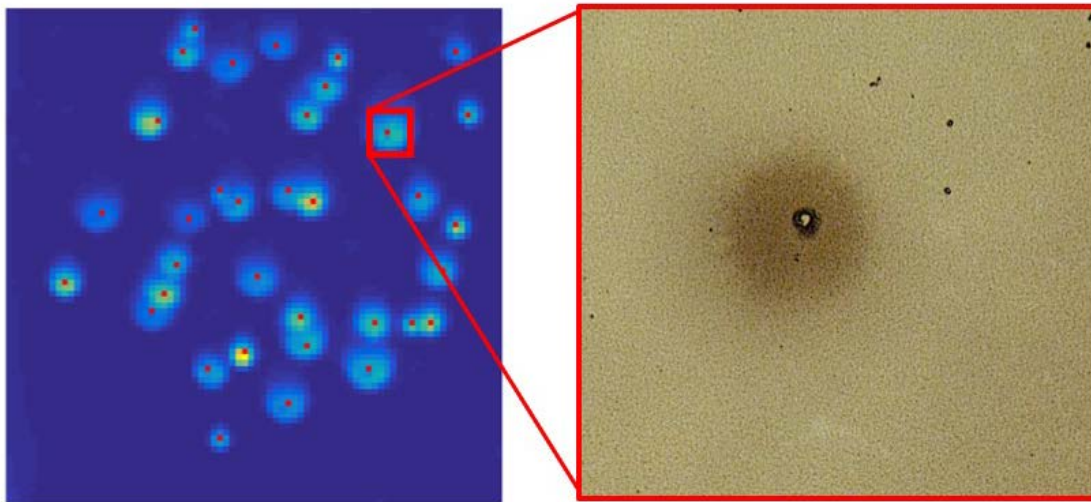


Figure 10. Nucleation site identification and validation using high-resolution optical microscope.

Next, an algorithm was developed using a MATLAB script to analyze the mean rate of change of the heat flux over a given video. Nucleation sites will experience the broadest fluctuation of heat flux throughout nucleate boiling. Periods of increased heat transfer will occur during the evaporation and quenching phases, while an extremely small heat flux will be present when the area is covered with vapor from the bubble dry spot.

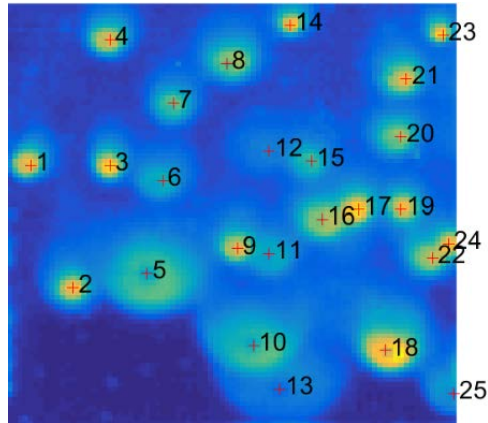


Figure 11. Typical output of nucleation site density analysis using IR data. The color scale is arbitrary.

The two methods have been compared and confirmed to indicate the presence of nucleation sites. While the microscope images are useful for measuring cavity size and overall geometry, only the IR analysis can yield active nucleation sites for a given test condition. The post-processed results, seen in Fig. 12, show a nucleation site density nearly two orders of magnitude less than what is predicted using well-known correlations [Hi2003]. This result is not unexpected as the ITO thin-film is nano-smooth. Only a few imperfections provide the micron-sized cavities necessary to function as nucleation sites.

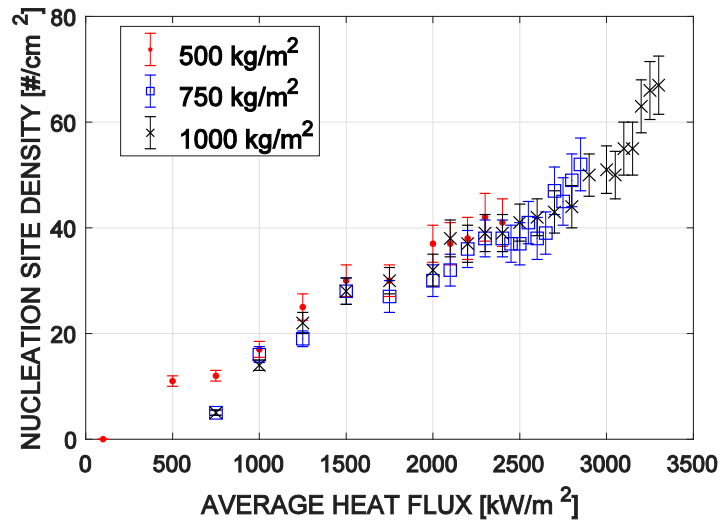


Figure 12. Nucleation site density

Once the nucleation sites have been identified, the temperature or heat flux time evolution can be analyzed to reveal the bubble period for each site individually. Similarly, the growth time and wait time can be measured using the same technique. The growth time is associated with a decrease in temperature and increase in heat flux due to the enhanced heat transfer from bubble nucleation. The wait time is then simply $t_w = t_b - t_g$.

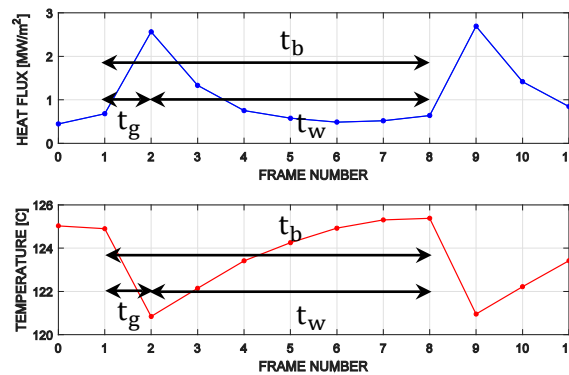


Figure 13. Illustration of bubble period, growth time and wait time.

Figure 14 shows the growth time and wait time as a function of applied heat flux. The wait time is reduced with increased heat flux, as expected, while the growth time remains constant. As the heat flux increases, the growth time becomes a greater fraction of the bubble period. This is consistent with conventional heat transfer arguments.

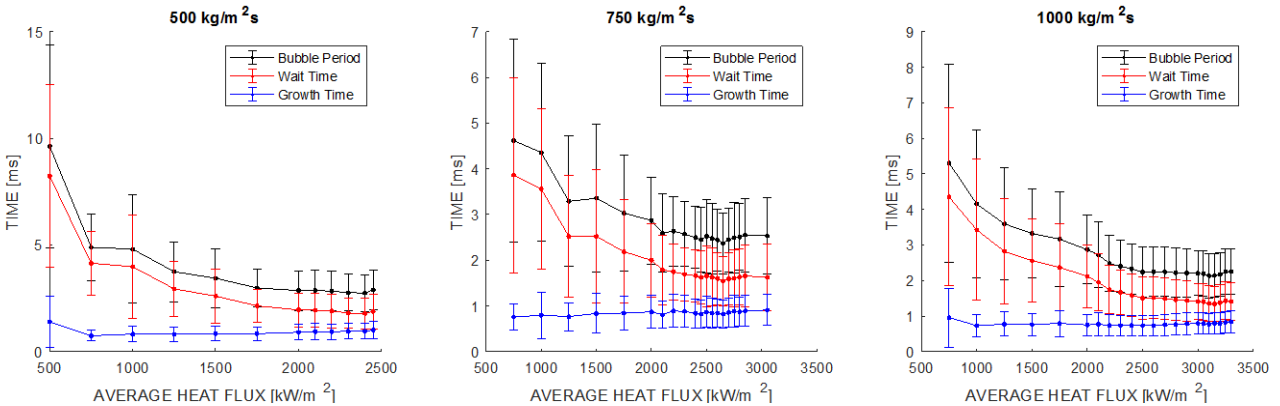


Figure 14. Bubble period, growth time and wait time as a function of applied heat flux.

6.2 Heat Flux Partitioning

This section outlines the algorithms and techniques used for identifying, isolating and quantifying the wall heat partitioning terms. The partitioning is accomplished by isolating the heat transfer mechanism based on the physics associated with each mechanism.

6.2.1 Dry Area Fraction

During bubble formation, as the micro-layer begins to evaporate, a dry spot forms at the base of the bubble. The collective area of the dry spots on the heated surface is referred to as the dry area fraction. This area has very little heat transfer due to the low heat transfer coefficient between the heated wall and the vapor.

To measure the dry area fraction, the heat flux distribution image (as in Fig 7.) can be analyzed to isolate the areas with very low heat transfer. Examples of these regions are circled white in the subfigure of Fig. 15. The region just to the outside of the dry area of the bubble is in contact with water. The ring separating these two regions is referred to as the triple-contact line, referencing the contact of all three phases, solid wall, liquid thin film, and dry vapor.

Figure 15 shows the increase in dry area with increasing heat flux. As the applied heat flux is increased, more nucleation sites are activated, nucleation frequency increases, and wait time decreases. This results in an increase in the total dry area fraction across the heater.

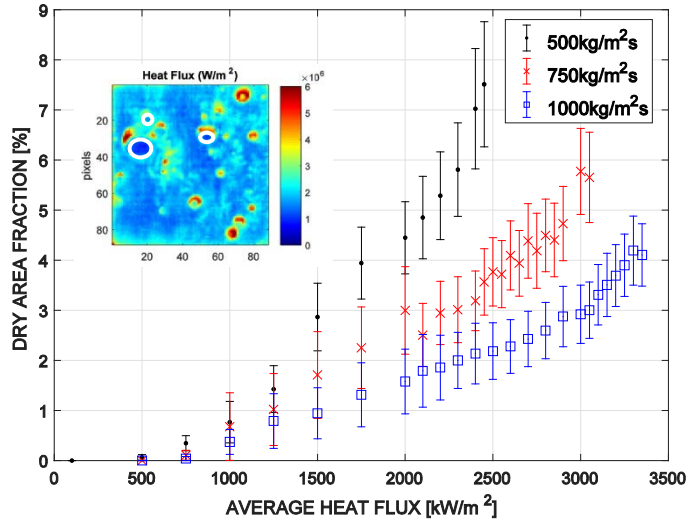


Figure 15. Dry area fraction as a function of applied heat flux.

The dry area fraction increases monotonically with increasing heat flux. However, the dry area never exceeds 10% of the total surface area, even just before CHF. Previous work by Kim et al. [Kim2013] showed that the dry area can be as high as 35% in pool boiling, with the same subcooling conditions.

6.2.2 Evaporative Heat Flux

The evaporation mechanism is associated with increased heat flux due to the large amount of heat required to trigger bubble growth and to evaporate the micro-layer underneath the bubble. Naturally, the algorithm begins by isolating areas of high heat flux. However, quenching also results in increased heat transfer due to cool liquid coming in contact with the heated wall. The HSV data is used to separate the quenching heat flux from the evaporation heat flux. The front-view of the heater provides the location of bubbles forming on the heater surface, essentially a bubble foot print. The bubble foot print can then be used as a mask for the heat flux image to separate the areas where the boiling surface is covered by bubbles. Then, a filter based on the heat flux level is applied to distinguish between areas where evaporation is actually occurring from regions where the bubbles are no longer in contact with the surface and heat transfer occurs without mass transfer. An example of the masking technique is depicted in Fig. 16.

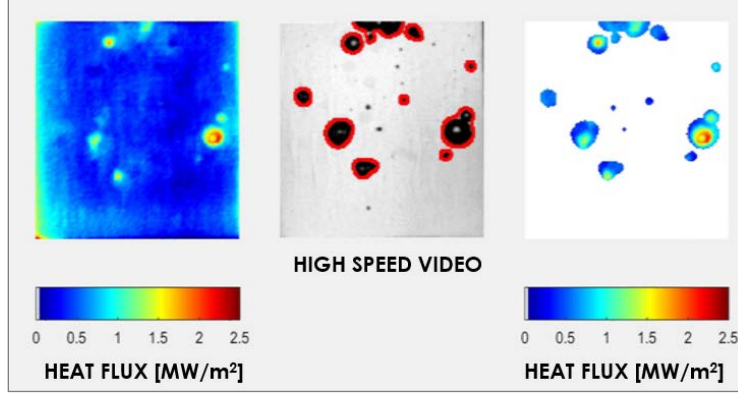


Figure 16. Bubble footprint mask for evaporation heat flux.

6.2.3 Single Phase Heat Flux

The remaining area, after the dry area and evaporation area have been identified, is attributed to single-phase heat transfer. The single-phase heat transfer, as it pertains to heat flux partitioning, consists of two terms, the forced convection term and the quenching term. The forced convection heat flux partitioning term was determined by using constant 2-D forced convection heat transfer coefficient distribution. The heat transfer coefficient distribution was obtained from the lowest heat flux data, where no boiling occurs. The only heat transfer mechanism in this regime is forced convection. The heat transfer coefficient distribution can be determined by averaging the heat transfer over all frames for each pixel, as shown in Eq. 1:

$$\overline{h_{fc}}(x,y) = \frac{1}{N} \sum_{t=1}^N \frac{q''(x,y,t)}{(T_w(x,y,t) - T_b)} \quad (1)$$

where N is the number of frames. Once the onset of nucleate boiling is reached, and the single-phase heat transfer area is determined, the forced convection heat flux partitioning term, q''_{fc} , can be determined by taking the time average of Eq. 2:

$$\frac{q''_{fc}(t)}{q''_{avg}} = \frac{1}{A_{tot}} \int_{A_{sp}} \overline{h_{fc}}(x,y) (T_w(x,y,t) - T_b) dA \quad (2)$$

Here q''_{avg} is the average applied heat flux, A_{tot} is the total area of the heater, A_{sp} is the area attributed to single-phase heat transfer, h_{fc} is the forced convection heat transfer coefficient and, T_w and T_b are the wall

and bulk temperatures, respectively. Here, it assumed that the presence of bubbles does not affect the forced convection heat transfer coefficient, an assumption that could be revisited in future, with more sophisticated treatments of the data.

Once nucleate boiling has been initiated, quenching also contributes to the single-phase heat transfer. The heat flux attributed to quenching over the wetted area can be calculated as shown in Eq. 5.

$$q_q''(x,y,t) = q_{sp}''(x,y,t) - q_{fc}''(x,y,t) \quad (3)$$

Thus, the heat transfer associated with the enhancement of single-phase heat transfer due to quenching and other possible enhancement mechanisms such as disturbance of the thermal boundary layer from movement of bubbles along the surface is calculated as the time average of

$$\frac{q_q''(t)}{q_{avg}} = \frac{1}{A_{tot}} \int_{A_{sp}} q_q''(x,y,t) dA \quad (4)$$

6.2.4 Heat Flux Partitioning Results

The complete heat flux partitioning is shown in Fig. 17. The green dots are the single-phase heat flux, blue is the forced convection heat flux, teal is the quenching heat flux, red is the evaporation heat flux, and black is the dry area heat flux. Note that the green dots (single phase) are the sum of blue (forced convection) and teal (quenching) dots.

Forced convection is the dominant term throughout the low and moderate heat fluxes. The forced convection term decreases monotonically, as is expected in current mechanistic nucleate boiling models. As more nucleation sites are activated at higher heat fluxes, there is a decrease in the single-phase heat transfer area. Interestingly, the quenching term increases initially as the heat flux is increased, then decreases before CHF is reached. The initial increase is attributed to the rise in nucleation site density, while the reduced relative contribution is due to a decrease in the growth time and average wetted area.

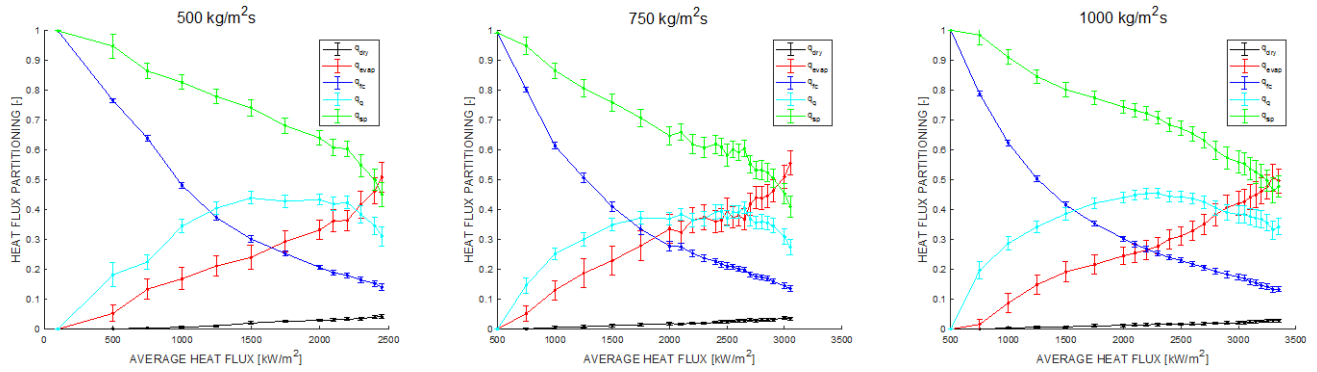


Figure 17. Heat flux partitioning of flow boiling at 10K subcooling, at atmospheric pressure for 500, 750 and 1000 kg/m²s.

The evaporative heat flux increases nearly monotonically with increasing applied heat flux. However, the evaporative heat flux is not the dominant term in the heat partitioning equation. In fact, evaporation never accounts for more than about 50% of the total heat flux. This result is contrary to the traditional heat partitioning models, e.g. Kurul and Podowski's, where evaporation is the dominant term [Kur1990]. It appears the evaporation is limited by the number of activated nucleation sites. As more sites are activated, closer to the CHF condition, evaporation does momentarily become the largest term.

7. High-Pressure Loop Shakedown Preliminary Results

The high-pressure loop has been constructed and preliminary tests have taken place. The loop has been operated at full capacity, 10 bars pressure and 180 °C temperature. Flow boiling images have been collected at 10K subcooling with 1, 2 and 5 bars pressure, 1000 kg/m²/s mass flow rate and 1250 kW/m² heat flux. These tests confirm the integrity of the heater and electrical connections at the elevated temperatures and pressures. High-speed video images of each of the conditions are shown in Fig. 18.

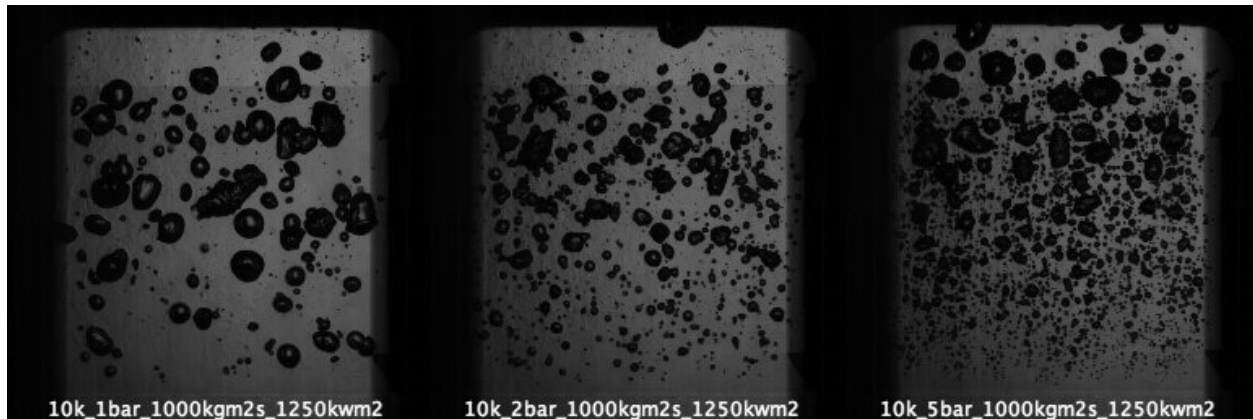


Figure 18. HSV images of flow boiling at 1 bar (left), 2 bar (center) and 5 bar (right) pressure.

8. Conclusions

A new flow boiling facility was designed, constructed and operated to generate data for validation of mechanistic boiling heat transfer models. IR and HSV cameras were employed to generate a new data set with high-resolution measurements. Post-processing algorithms were developed to analyze the time-dependent heat flux and temperature distributions to extract governing boiling parameters such as the nucleation site density, bubble frequency, growth and wait times and dry area fraction. Additionally, algorithms were developed to identify and quantify the partitioned heat fluxes for each heat transfer mechanism.

Experimental results show that, in our experiments, the evaporation term in the partitioned heat flux is not as significant as previously hypothesized. Single-phase forced convection is the dominant mechanism for much of the nucleate boiling curve, whereas evaporation becomes the largest term only before CHF. This appears to be due to relatively small number of active nucleation sites on the heater surface, which is almost two orders of magnitude less than what is estimated using well-known correlations such as the Hibiki and Ishii's [Hi2003].

Moving forward, much of the work to be done will focus on incorporating high-pressure testing to see the effect of pressure on heat flux partitioning. Additionally, further refinement of the post-processing algorithms can yield additional data on the sliding conduction term to validate newly proposed mechanistic models.

Reference

- [Bu2016] Matteo Bucci, Andrew Richenderfer, Guan-Yu Su, Thomas McKrell, Jacopo Buongiorno, “A mechanistic IR calibration technique for boiling heat transfer investigations”, *International Journal of Multiphase Flow*, vol.83, pag.115-127 (2016)
- [Gr2007] D.C. Groeneveld, J.Q. Shan, A.Z. Vasic, L.K.H. Leung, A. Durmayaz, J. Yang, S.C. Cheng, A. Tanase, “*The 2006 CHF look-up table*”, *Nuclear Engineering and Design*, vol.237, pag.1909-1922 (2007).
- [Su2016] Guan-Yu Su, Matteo Bucci, Thomas McKrell, Jacopo Buongiorno, “*Transient boiling of water under exponentially escalating heat inputs. Part I: Pool Boiling*”, *International Journal of Heat and Mass Transfer*, vol.96, pag.667-684 (2016).
- [Su2016b] Guan-Yu Su, Matteo Bucci, Thomas McKrell, Jacopo Buongiorno, “*Transient boiling of water under exponentially escalating heat inputs. Part II: Flow Boiling*”, *International Journal of Heat and Mass Transfer*, vol.96, pag.685-698 (2016).
- [Hi2003] T. Hibiki and M. Ishii, “*Active nucleation site density in boiling systems*”, *International Journal of Heat and Mass Transfer*, vol. 46(14), pag. 2587 – 2601, 2003.
- [Kim3013] H. Kim, Y. Park and J. Buongiorno, “*Measurement of wetted area fraction in subcooled pool boiling of water using infrared thermography*,” *Nuclear Engineering and Design*, vol. 264, pag. 103–110, 2013.
- [Kur1990] N. Kurul and M. Z. Podowski, “*Multidimensional effects in forced convection subcooled boiling*,” in *Proceedings of the 9th International Heat Transfer Conference*, Jerusalem, 1990.